Journal of Solid State Chemistry 181 (2008) 2776–2782

Contents lists available at ScienceDirect

Journal of Solid State Chemistry

journal homepage: www.elsevier.com/locate/jssc

Anomalous low-temperature behavior of the Co dimers in the oxo-halide $CoSb_2O_3Br_2$

Zuzana Hugonin [a,1], Mats Johnsson [a,*], Sven Lidin [a,1], Dirk Wulferding [b,2], Peter Lemmens [b,2], Reinhard K. Kremer [c,3]

[a] Department of Inorganic Chemistry, Stockholm University, S-106 91 Stockholm, Sweden
[b] Institute for Condensed Matter Physics, TU Braunschweig, D-38106 Braunschweig, Germany
[c] Max Planck Institute for Solid State Research, Heisenbergstrasse 1, D-70569 Stuttgart, Germany

ARTICLE INFO

Article history:
Received 11 April 2008
Received in revised form
3 July 2008
Accepted 9 July 2008
Available online 15 July 2008

Keywords:
Oxo-halide
Crystal structure determination
Lone-pair elements
Magnetic susceptibility
Raman scattering
Inversion symmetry

ABSTRACT

We report the synthesis, crystal structure determination, magnetic and low-temperature structural properties of a new cobalt antimony oxo-bromide. $CoSb_2O_3Br_2$ crystallizes in the triclinic crystal system, space group $P\bar{1}$, with the following lattice parameters: $a = 5.306(3)$ Å, $b = 7.812(4)$ Å, $c = 8.0626(10)$ Å, $\alpha = 88.54(3)^\circ$, $\beta = 82.17(3)^\circ$, $\gamma = 80.32(4)^\circ$, and $Z = 2$. The crystal structure was solved from single crystal X-ray data and refined on F^2, $R_1 = 3.08$. The structure consists of layers made up by three building blocks, $[CoO_4Br_2]$, $[SbO_3Br]$, and $[SbO_3]$ that are connected via edge- and corner-sharing so that structural Co–Co dimers are formed. The layers have no net charge and are only weakly connected by van der Waals forces to adjacent layers. Above ~25 K the magnetic susceptibility is independent of the magnetic field and can be very well described by a Curie–Weiss law. Below 25 K the susceptibility passes through a maximum and decreases again that is typical for the onset of long-range antiferromagnetic correlations. Long-range antiferromagnetic ordering is observed below T_N~9 K indicating substantial inter-dimer exchange coupling between Co–Co dimers within the layers. However, according to the heat capacity results only a minute fraction of the entropy is associated with the long-range ordering transition. The phonon anomalies observed for $T < 6$ K in Raman scattering and an anomaly in the specific heat point to a structural instability leading to a loss of inversion symmetry at lowest temperatures.

1. Introduction

A synthesis concept developed for searching new low-dimensional magnetically frustrated inorganic compounds has successfully been applied during the past years [1–7]. The concept is based on forming oxo-chlorides/oxo-bromides comprising *p*-element cations that carry a stereochemically active lone-pair of electrons (e.g. Te^{4+}, Se^{4+}, Sb^{3+}). The nature and the steric requirements of the lone-pair will cause one-sided coordination around the lone-pair cation [8]. The *p*-element lone-pair cations are most often bonded only to oxygen atoms in oxo-bromides/oxo-chlorides due to their high Lewis acid strength. Late transition metal cations introduced to lone-pair element oxo-halide systems display more affinity for halides [1–7]. It is found to be common in our previous studies on oxo-halides that chlorine/bromine ions form only a single bond and act as terminating species that reside together with the lone-pairs in large non-bonding regions in the structure [9,10]. Hence, the combination of lone-pairs and halide ions is an efficient tool in order to open up the crystal structures and to increase the possibility for finding new low-dimensional arrangements. In this way also the magnetic dimensionality is influenced that may create unusual magnetic behavior.

The search for novel low-dimensional compounds in the Co^{2+}–Sb^{3+}–O–X (X = halide ion) system resulted in the new compound $CoSb_2O_3Br_2$. To the best of our knowledge it is the first described Co^{2+} containing antimony oxo-halide. $CoSb_2O_3Br_2$ comprises structural Co^{2+}–Co^{2+} dimers reminding of the Cu^{2+}–Cu^{2+} dimers in $CuTe_2O_5$ that are also isolated by surrounding lone-pair cations [11,12].

2. Experimental

Single crystals and powder of $CoSb_2O_3Br_2$ were obtained in sealed evacuated silica tubes from Sb_2O_3 (Sigma-Aldrich, 99%) and

* Corresponding author. Fax: +46 8 15 21 87.
E-mail addresses: zuzana@inorg.su.se (Z. Hugonin), matsj@inorg.su.se (M. Johnsson), sven@inorg.su.se (S. Lidin), d.wulferding@tu-bs.de (D. Wulferding), p.lemmens@tu-bs.de (P. Lemmens), rekre@fkf.mpg.de (R.K. Kremer).
[1] Fax: +46 8 15 21 87.
[2] Fax: +49 531 391 5155.
[3] Fax: +49 711 689 16 89.

0022-4596/$ - see front matter © 2008 Elsevier Inc. All rights reserved.
doi:10.1016/j.jssc.2008.07.005

$CoBr_2$ (Research chemicals Ltd, 98%). Mixtures of Sb_2O_3 and $CoBr_2$ in a molar ratio of 1:1 were heat treated in a muffle furnace at 400 °C for 192 h, the amount of starting materials was 0.3 g. The synthesis product contained dark blue $CoSb_2O_3Br_2$ single crystals and dark blue crystalline powder of the same phase. The fraction of single crystals was about 10% and the rest powder. Attempts were made to synthesize $CoSb_2O_3Cl_2$ and $CoSb_2O_3I_2$ with similar methods, however those attempts where not successful.

The chemical composition of the new oxo-halide was characterized in a scanning electron microscope (SEM, JEOL 820) equipped with an energy-dispersive spectrometer (EDS, LINK AN10000).

Single crystal X-ray diffraction data were collected on an Oxford Xcalibur3 system, mounted with a Mo$K\alpha$ source. Integration of the reflection intensities and absorption correction were made using the software provided by the diffractometer manufacturer [13]. The structure was solved by direct methods (SHELXS97) [14] and refined by full matrix least squares on F^2 using the program SHELXL97 [15]. All illustrations were made with the program DIAMOND [16]. Crystallographic data for $CoSb_2O_3Br_2$ are shown in Table 1.

The samples used for susceptibility and heat capacity measurements where characterized by powder X-ray diffraction using a Guiner-Hägg focusing camera with subtraction geometry (Cu$K\alpha_1$ $\lambda = 1.54060$ Å). Silicon, $a = 5.430088(4)$ Å, was added as an internal standard. The recorded films were read in an automatic scanner and the data were evaluated using the program SCANPI [17] and PIRUM [18].

The magnetic susceptibilities of a polycrystalline sample ($m \sim 40$ mg) were measured in a MPMS SQUID magnetometer (Quantum Design) at various external fields in the temperature range $1.8\,K \leqslant T \leqslant 300\,K$. The heat capacities were determined in a PPMS system (Quantum Design) in the temperature range $1.8\,K \leqslant T \leqslant 50\,K$ in magnetic fields up to 6 T on a randomly oriented polycrystalline sample of ~2 mg. The addenda heat capacities of a minute amount of Apiezon N grease used to thermally couple the sample to the platform and the heat capacity of the platform were determined in a separate run and subtracted.

Raman scattering experiments were performed in quasi-backscattering geometry with a laser power of $P = 0.5$ mW at $\lambda = 532$ nm excitation wavelength and a focus diameter of $d = 100\,\mu m$. Small single crystal samples of $CoSb_2O_3Br_2$ were attached to a cold finger of an evacuated cryostat allowing a temperature variation between 3.1 and 300 K. No evidence for changes in the Raman spectra was found for temperatures above 10 K. Therefore, we focussed our attention on the Raman spectra collected below 10 K. There was no evidence of polarization effects in the spectra. This is related to the symmetry of the excitations.

Table 1
Crystal data for $CoSb_2O_3Br_2$

Formula weight	510.25
Temperature (K)	293(2)
Wavelength (Å)	0.71069
Crystal system	Triclinic
Space group	$P\bar{1}$
Unit cell dimensions (Å, deg)	$a = 5.306(3)$, $\alpha = 88.54(3)$
	$b = 7.812(4)$, $\beta = 82.17(3)$
	$c = 8.0626(10)$, $\gamma = 80.32(4)$
Volume (Å^3)	326.3(3)
Z	2
Density (calc) (g/cm^3)	5.193
Adsorption coefficient (mm^{-1})	22.89
Absorption correction	Multi-scan
$F(000)$	446
Crystal color	Dark blue
Crystal habit	Plate like
Crystal size	$0.04 \times 0.04 \times 0.02$
θ range for data collection (deg)	4.36–27.10
Index range	$-6 \leqslant h \leqslant 6$, $-9 \leqslant k \leqslant 10$ $-10 \leqslant l \leqslant 10$
Reflections collected	7126
Independent reflections	1421 [R(int) = 0.0702]
Completeness to θ	0.991
Refinement method	Full-matrix least squares on F^2
Data/restraints/parameters	1421/0/73
Goodness-of-fit on F^2	0.964
Final R indices [$I > 3\sigma(I)$]	$R = 0.0308$
	w$R = 0.0652$
R indices (all data)	$R = 0.0437$
	w$R = 0.0659$
Largest difference peak and hole	1.204 and −1.256 (e Å^{-3})

3. Results and discussion

3.1. Crystal structure

The new layered compound $CoSb_2O_3Br_2$ crystallizes in the triclinic system, space group $P\bar{1}$, and the layers extend in the ac-plane. EDS analyses based on 6 different crystals confirm the presence and stoichiometry of the heavy elements to be 41.6±1.4 at% Sb, 21.6±2.1 at% Co, 36.8±2.7 at% Br. The silicon content is at the detection limit for the instrument indicating that there was no substantial reaction with the silica tubes. Those values are in reasonable agreement with the structural refinement that gives 40 at% Sb, 20 at% Co, and 40 at% Br. The bromide ions and the lone-pairs of electrons E belonging to Sb^{3+} cation, protrude from the layers into non-bonding regions of the structure, see Fig. 1. The shortest cation–anion distances between adjacent layers; Sb(1)···Br(2) = 3.79(6) Å, Sb(2)···Br(2) = 4.24(7) Å are markedly longer than the cation–cation separation within the layers; Sb(2)···Sb(2) = 3.18(5) Å, Sb(1)···Sb(1) = 3.26(3) Å, Co(1)···Co(1) = 3.39(1) Å. The cation–cation separation within the layers are of about the same distances as the cation–anion interlayer distances indicating absence of significant bonding contact in between the adjacent layers and suggest that only weak van der Waals forces connect the layers to each other in the structure. Each layer may thus be considered as an infinite two-dimensional neutral molecule.

Bond valence sum (BVS) calculations were used as a guide to decide which ligands should be considered as belonging to the primary coordination sphere of Sb^{3+}. The bond valence contribution for each atom is listed in Table 2 and BVS for each of the ligands can be found in Table 3.

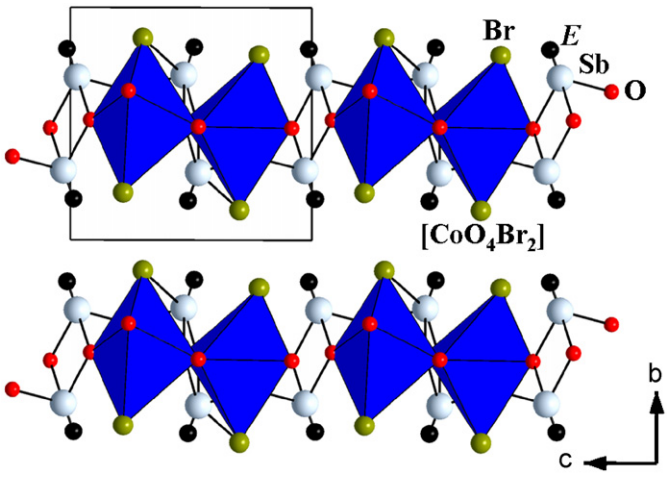

Fig. 1. Structure of $CoSb_2O_3Br_2$ viewed along the a-axis. The layers are separated by non-bonding volumes occupied by bromide ions and stereochemically active lone-pair electrons of Sb^{3+}.

Table 2
Atomic coordinates, equivalent isotropic displacement parameters, and bond valence sum for $CoSb_2O_3Br_2$

Atom	*x*	*y*	*z*	*U*(eq)[a]	BVS[b]
Sb1	0.0696(1)	0.29090(8)	0.47027(7)	0.0163(2)	2.96
Sb2	−0.8960(1)	1.29998(8)	0.02824(7)	0.0161(2)	2.98
Br1	−0.6526(2)	0.7950(1)	0.2181(1)	0.0265(2)	0.66
Br2	−0.2539(2)	0.1307(1)	0.3002(1)	0.0252(2)	0.84
Co1	−0.4761(2)	0.4829(2)	0.2889(1)	0.0160(3)	1.89
O1	−0.233(1)	0.4883(8)	0.4698(7)	0.018(1)	2.02
O2	−0.776(1)	1.3583(8)	0.2403(7)	0.017(1)	2.19
O3	−0.785(1)	1.5171(8)	−0.0832(7)	0.019(1)	2.12

[a] *U*(eq) is defined as one-third of the trace of the orthogonalized *U* tensor.
[b] Bond valence sum calculations have been performed according to Brown and Altermatt [26]. $r_0 = 1.973$ for Sb^{3+}–O bonds [26], 2.51 for Sb^{3+}–Br bonds [27], 1.692 for Co^{2+}–O bonds [26] and 2.196 for Co^{2+}–Br bonds [28].

Table 3
Selected geometric parameters and bond valence for $CoSb_2O_3Br_2$

	Bond distance (Å)	Bond valence
Sb1–O1	2.030(6)	0.86
Sb1–O1^{ii}	2.148(6)	0.62
Sb1–O2^{i}	2.016(6)	0.89
Sb1–Br2	2.800(2)	0.46
Sb1–Br1	3.249(1)	0.14
Sb2–O2	1.991(5)	0.95
Sb2–O3^{iii}	2.029(6)	0.86
Sb2–O3	2.036(6)	0.84
Sb2–Br2	3.116(1)	0.19
Sb2–Br1	3.277(1)	0.13
Co1–O1	2.081(5)	0.35
Co1–O1^{vi}	2.304(5)	0.19
Co1–O2^{v}	2.087(5)	0.34
Co1–O3^{iv}	2.012(5)	0.42
Co1–Br1	2.540(2)	0.40
Co1–Br2	2.810(2)	0.20

Symmetry codes: (i) 1+*x*, −1+*y*, *z*; (ii) −*x*, 1−*y*, 1−*z*; (iii) −2−*x*, 3−*y*, −*z*; (iv) −1−*x*, 2−*y*, −*z*; (v) *x*, −1+*y*, *z*; (vi) −1−*x*, 1−*y*, 1−*z*.

Sb(1) is four-coordinated by three oxygen and one bromine atom. The shortest Sb(1)–Br(2) distance, 2.800(2) Å, corresponds to a bond valence of 0.46 and this large contribution indicates that the bromine atoms must be considered as bonded. This finding is rather unexpected as the shortest Sb–*X* distance in previously described *M*–Sb–O–*X* compounds (*M* = metal cation, *X* = halide anion) are too long to be considered as belonging to the primary coordination sphere around Sb^{3+} [9,10,19]. However, it has been observed previously in oxo-halides that the lone-pair element bond directly to a halide ion [6]. When taking also the lone-pair electrons, *E*, into account a distorted trigonal bipyramid, [Sb(1)O_3Br*E*] is formed, with antimony atoms preserving its one-sided coordination. The next set of Sb–Br distances is found in the range between 3.116(1) and 3.277(1) Å providing very small contributions to the cation valence, see Table 3, and consequently these bromine atoms are therefore not considered as bonded. Sb(2) is three-coordinated by oxygen atoms and a distorted [Sb(2)O_3*E*] tetrahedron is formed. The Co^{2+} atom has a distorted octahedral [CoO_4Br_2] coordination with oxygen atoms in the equatorial plane and bromine atoms at the axial positions. The two Br ions contribute differently to its bond valence, see Table 3. A stronger Co–Br bond is formed to Br(1) atoms while Br(2) shows a stronger interaction with Sb(1) atoms as discussed above.

A unique feature in the crystal structure of $CoSb_2O_3Br_2$ is the presence of isolated pairs of edge-sharing [CoO_4Br_2] octahedra. The Co–Co intra-dimer distance amounts to 3.39(1) Å, see Fig. 2. The structural dimers are well separated as the shortest distance in between two Co atoms belonging to different dimers in the same layer is 4.699(1) Å. The closest distance between two Co atoms in different layers is 7.812(4) Å.

All the polyhedra in $CoSb_2O_3Br_2$ are substantially distorted. The deformation of the [SbO_3E] tetrahedra and the [SbO_3BrE] bipyramids can be partly assigned to the presence of the unshared electron pair [20]. The second contributing factor is the electrostatic repulsion in between the cations of the edge-sharing polyhedra in the $[CoSb_2O_3Br_2]_\infty$ layers. The two [CoO_4Br_2] octahedra building the structural dimer have a common equatorial edge and each of these polyhedra further share an equatorial and an axial edge with two different [Sb(1)O_3Br*E*] bipyramids. The structure can be viewed as being formed by stripes of alternating pairs of [CoO_4Br_2] and pairs of [SbO_3BrE] that propagate along the *a*-axis. Such stripes are linked by corner sharing to [$Sb_2O_4E_2$] groups that in turn are made up of edge-sharing [Sb(2)O_3E] tetrahedra, see Fig. 3.

Assigning $CoSb_2O_3Br_2$ to the triclinic space group $P\bar{1}$ (2) with two formula units per unit cell ($Z = 2$) allows a symmetry analysis with respect to the Raman and infrared (IR) active phonons. All 8 atoms occupy lowest symmetry sites (2i). This leads to 3 modes in Raman active A_g and 3 in IR active A_u symmetry for each atom,

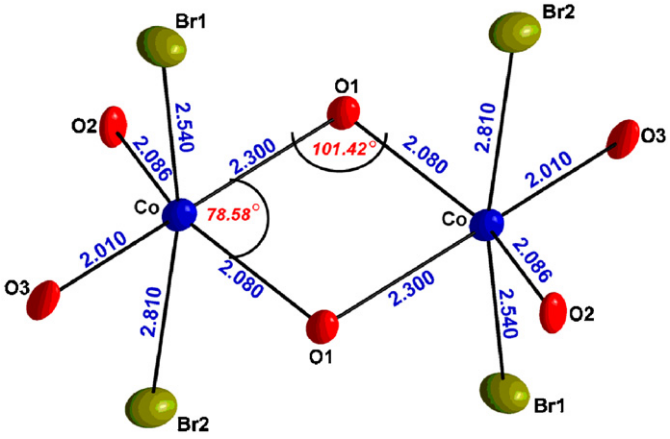

Fig. 2. The Co–Co dimer is built from two edge sharing distorted [CoO_4Br_2] octahedra.

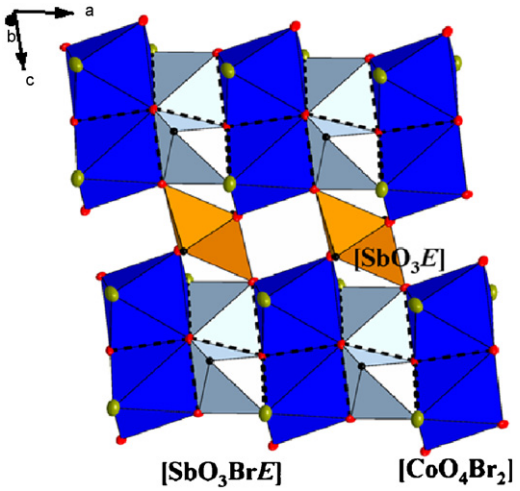

Fig. 3. Edge-sharing distorted [CoO_4Br_2] octahedra and [Sb(1)O_3Br*E*] trigonal bipyramids form stripes extending in the *a*-direction. A $[CoSb_2O_3Br_2]_\infty$ layer is formed by connecting the stripes by corner-sharing to [$Sb_2O_4E_2$] groups that in turn are made up of edge-sharing [Sb(2)O_3E] tetrahedra.

adding up to 24 Raman active vibrations [21]. The same total number of phonons is IR active. Owing to the low symmetry of the atom positions the A_g Raman tensor has only nonzero elements. Together with the large number of expected phonon modes the Raman spectra are therefore expected to be very unspecific, i.e. phonons are observed without selective light scattering polarizations.

3.2. Magnetic properties

The powder sample used for the magnetic susceptibility and the heat capacity measurements was characterized by powder X-ray diffraction measurements. These confirmed a triclinic unit cell with lattice parameters in good accordance with the results found from the single crystal determination: $a = 5.482(34)$ Å, $b = 7.574(39)$ Å, $c = 8.100(23)$ Å, $\alpha = 89.45(93)^\circ$, $\beta = 82.17(50)^\circ$, $\gamma = 80.60(38)^\circ$.

Two representative measurements of the reciprocal magnetic susceptibility of $CoSb_2O_3Br_2$ collected in external fields of 0.1 and 1 T are shown in Fig. 4. Above ~25 K the magnetic susceptibility is independent of the magnetic field and can be very well described by a Curie–Weiss law:

$$\chi_{mol} = \frac{C}{(T-\Theta)} + \chi_0$$

with a Curie constant $C = 1.95(1)\,cm^3\,K/mol$ corresponding to an effective magnetic moment $\mu_{eff} = 3.95(1)\,\mu_{Bohr}$. In the fits, we fixed $\chi_0 = \chi_{dia}$, with $\chi_{dia} = -156 \times 10^{-6}\,cm^3/mol$, corresponding to the sum of the diamagnetic increments of the constituting elements in their respective oxidation states according to Selwood: Co^{2+}: $-12 \times 10^{-6}\,cm^3/mol$; Sb^{3+}: $-17 \times 10^{-6}\,cm^3/mol$; O^{2-}: $-12 \times 10^{-6}\,cm^3/mol$; Br^-: $-36 \times 10^{-6}\,cm^3/mol$ [22].

The Curie–Weiss temperature amounts to $\theta = -44.0(5)$ K, indicating predominant antiferromagnetic exchange interaction. Below 25 K, the susceptibility passes through a maximum and decreases again, indicating the built-up of antiferromagnetic correlations. The shape of the anomaly and the magnitude depend on the strength of the magnetic field (Fig. 5c). At the lowest field ($B = 0.1$ T), the susceptibility passes through a rounded plateau and exhibits a shoulder at about 10 K. At 0.1 T field-cooled (fc) and zero field-cooled (zfc) susceptibility are split below ~17 K. For higher fields the fc–zfc splitting disappears and the plateau is rounded with the resulting broad maximum shifted to lower temperatures.

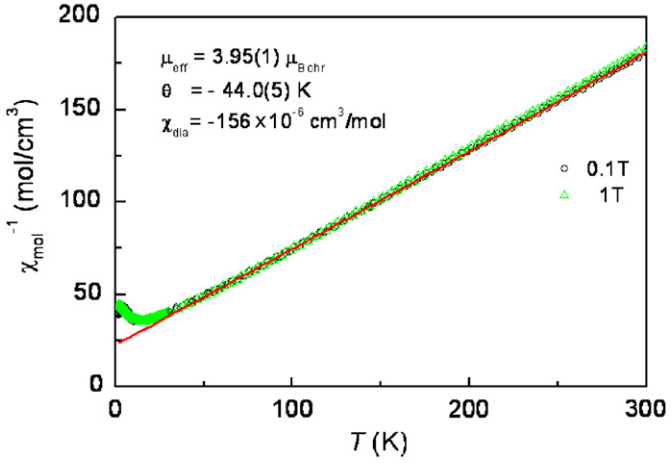

Fig. 4. Reciprocal magnetic susceptibility of $CoSb_2O_3Br_2$ measured in external fields of 0.1 and 1 T, as indicated in the inset. The red solid line represents a Curie–Weiss law $\chi_{mol} = C/(T-\theta)+\chi_{dia}$, with parameters given in the insert. The Curie constant is defined in the usual way according to $C = N_A\mu_{Bohr}^2\mu_{eff}^2/3k_B$.

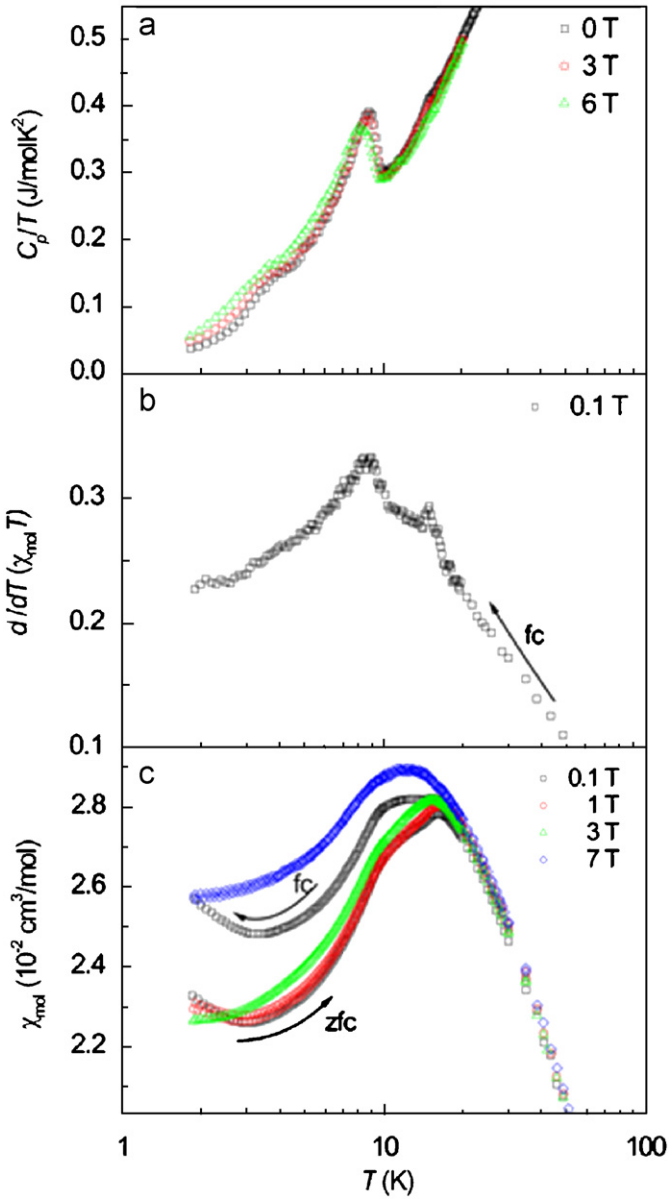

Fig. 5. (a) Heat capacity, (b) 'Fishers heat capacity', $d/dT(\chi_{mol}T)$, (see text) and (c) magnetic susceptibility of $CoSb_2O_3Br_2$ measured in external magnetic fields as indicated in the insets. The arrows in (b) and (c) give the direction of temperature change. The zero field-cooled (zfc) data were measured with increasing temperature after the sample had been cooled to 1.8 K in zero field. The field-cooled data were collected with decreasing temperature with magnetic field applied. In (c) only the 0.1 T data show a marked splitting of the fc and zfc data, while at all other fields the fc and zfc data are identical.

The anomalies observed in the temperature dependence of the magnetic susceptibility are paralleled by anomalous features in the heat capacity (Fig. 5a) centered at ~15 and ~9 K.

The anomaly at ~15 K flattens with increasing field, while the 9 K λ-type anomaly shifts to lower temperatures. An additional broad sluggish feature at ~3.5 K is rather insensitive to magnetic fields. The entropy removed in the λ anomaly at 9 K amounts to ~0.6 J/mol/K.

Similar anomalies near 9 and 15 K are also seen in the quantity $d/dT(\chi_{mol}T)$ (Fisher's heat capacity), see Fig. 5b [23]. An anomaly near 3 K, however, is absent. We therefore attribute the heat capacity feature observed at this temperature to lattice degrees of freedom based on the observed phonon anomalies in Raman scattering (see below).

The magnetic susceptibility measurements indicate that Co^{2+} ($3d^7$ electronic configuration) in $CoSb_2O_3Br_2$ exhibits essentially spin-only magnetism associated to the spin value $S=\frac{3}{2}$ with a g factor $g=2.04$, slightly increased over the free ion value. Spin-only magnetism with $S=\frac{3}{2}$ corresponding to a $^4A_2$ ground state is usually expected for tetrahedral crystal field symmetry cf. e.g. [24]. The behavior of the magnetic susceptibility of $CoSb_2O_3Br_2$ is somewhat surprising in view of the (distorted) octahedral coordination geometry for Co in $CoSb_2O_3Br_2$ and not understood at the moment.

By using the relation

$$\theta = \frac{2}{3}S(S+1)\sum_i z_i J_i$$

the Curie–Weiss temperature θ can be related to the sum of the exchange parameters J_i to the moments in the ith neighboring shell comprising z_i Co atoms. From the experimental observation, $\theta=-44$ K, one obtains $\sum_i z_i J_i=-17.6$ K. If exchange takes place essentially between Co ions within a structural dimer, i.e. $z_1=1$ one estimates an intra-dimer exchange constant $J_1=J_{intra}=-17.6$ K. Assuming a dominant intra-dimer exchange coupling is supported by the finding that the entropy (~0.6 J/mol K, see above) associated to the heat capacity anomaly at 9 K, the onset of long-range ordering, contains only a minute fraction of the entropy expected for a $S=\frac{3}{2}$ system ($R\ln 4=11.5$ J/mol K). In a magnetic dimer with $S_1=S_2=\frac{3}{2}$ coupled with isotropic Heisenberg exchange according to $H=-2J_{intra}\vec{S}_1\vec{S}_2$ in case of antiferromagnetic exchange J_{intra} has a non-magnetic singlet ground state and a series of excited states that can be characterized by the total spin $S^T=0$, 1, 2, 3. On decreasing temperature entropy is removed by gradually depopulating the excited spin states.

The magnetic susceptibility (per one spin center) for a magnetic dimer formed by two $S=\frac{3}{2}$ magnetic centers is given by Eq. (1) with $x=J_{intra}/k_BT$ [25]:

$$\chi_{dimer}=\frac{N_A g^2\mu_{Bohr}^2}{k_BT}\frac{e^{2x}+5e^{6x}+14e^{12x}}{1+3e^{2x}+5e^{6x}+7e^{12x}} \quad (1)$$

Assuming an intra-dimer exchange constant of $J_{intra}=-17.6$ K, however, results in significant deviations between the measured data and the susceptibility calculated according to Eq. (1) (see dashed curve in Fig. 6). On the other hand, long-range antiferromagnetic ordering observed at T_N~9 K indicates substantial exchange coupling between the dimers. In fact, a significantly improved agreement of the experimental and calculated susceptibilities can be achieved if an additional inter-dimer exchange is taken into account. Fig. 6 shows the calculated susceptibility using a molecular-field modification of the dimer susceptibility according to (Eq. (2)):

$$\chi'_{mol}(T)=\frac{\chi_{dimer}(T)}{1-(2z_{inter}J_{inter}/N_A g^2\mu_{Bohr}^2)\chi_{dimer}(T)} \quad (2)$$

In Eq. (2), J_{inter} represents the inter-dimer exchange to z_{inter} neighbors. The best fit (see Fig. 6) results in an intra-dimer exchange of J_{intra}~−4.5 K. The quantity $2z_{inter}J_{inter}$ amounts to ~−11.8 K using $g=2.04$ and $\chi_{dia}=-156\times10^{-6}$ cm^3/mol as obtained from the Curie–Weiss fit of the high temperature reciprocal susceptibility data.

According to the structure analysis, each dimer is coupled to eight neighbor dimers within a layer. Since the transfer paths are different, the inter-dimer exchange to different types of neighbors will be different. In a simplified picture we may assume $z_{inter}=8$ and all inter-dimer exchange to be identical, the average inter-dimer exchange constant amounts to ~−0.7 K. According to this analysis $CoSb_2O_3Br_2$ can be described as a magnetic dimer, however, with essential inter-dimer exchange within the layers being present.

3.3. Raman scattering

In the Raman spectra of $CoSb_2O_3Br_2$ we identify 24 modes in the frequency regime in the range 30–700 cm^{-1}, see Fig. 7 [29]. Some shoulders and features with smaller intensity have been discarded in our analysis. Nevertheless, the good agreement with the symmetry analysis giving 24 Raman active modes supports the structure analysis and the validity of light scattering selection rules in $CoSb_2O_3Br_2$.

The modes can be classified into three groups according to their frequencies with very similar frequency separations and line widths. These groups are found in the frequency ranges of 30–110, 120–300 and 360–700 cm^{-1}, respectively. The line width of the phonons in the high frequency group is generally larger compared to those of the low frequency phonons. The former modes are most likely related to Co–O vibrations of the dimer coordination.

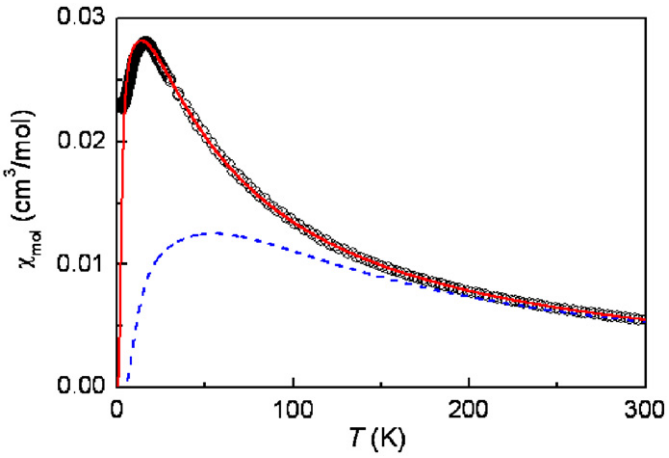

Fig. 6. Magnetic susceptibility of $CoSb_2O_3Br_2$ ($B=1$ T) compared with the magnetic susceptibility of a magnetic dimer consisting of two $S=\frac{3}{2}$ entities coupled by an isotropic Heisenberg exchange with an intra-dimer exchange constant of −17.6 K (blue dashed line). The (red) solid line results from a fit of the susceptibility of a $S=\frac{3}{2}$ dimer (Eq. (1)) modified according to (Eq. (2)) to take into account also inter-dimer exchange into account. The fitted intra-dimer and inter-exchange constants amount to $J_{intra}=-4.5$ K and $2z_{inter}J_{inter}=-11.8$ K, respectively.

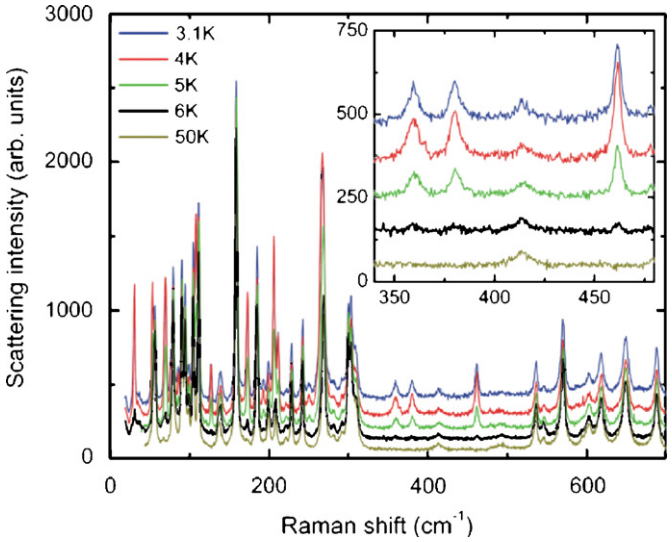

Fig. 7. Raman spectra of $CoSb_2O_3Br_2$ as function of temperature in the frequency regime from 30 to 700 cm^{-1}. The inset zooms into the intermediate frequency regime.

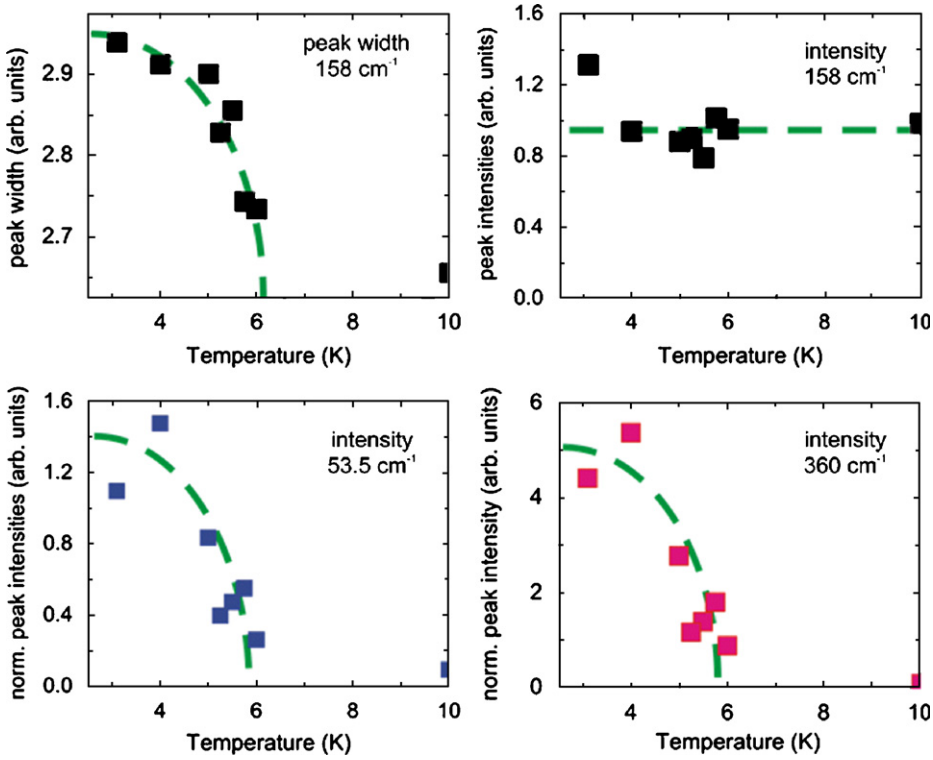

Fig. 8. Temperature dependence of peak width and intensity of some modes as function of temperature. The dashed line is a guide to the eye.

We have intensively investigated the temperature regime where specific heat and susceptibility data give evidence for a critical behavior of $CoSb_2O_3Br_2$. Anomalies are observed only below ~6 K. The inset of Fig. 7 shows a magnification of the intermediate frequency regime where high and low-temperature modes can be observed separately. Approximately 16 modes newly appear and increase in intensity without a large shift in frequency [30]. Some of the modes appear as shoulders with lower intensity in the proximity to high temperature modes. The overlap and the low intensity render a clear identification very difficult. In Fig. 8 we show the temperature evolution of line width and intensity of some modes. The temperature dependence is very similar for all modes. Additionally, one high temperature mode with approximately constant intensity at 158 cm^{-1} increases similarly in line width with decreasing temperatures. Finally, in the lowest frequency regime (30–50 cm^{-1}) a broader mode or background exists that is superimposed by a sharp mode at 35 cm^{-1}. We assign all modes with the exception of the broad continuum to optical phonon modes.

The broad continuum in the low frequency regime is a candidate for magnetic Raman scattering. Such a scattering process involves the simultaneous flip of spins on two adjacent dimers. For the coupled $S=\frac{1}{2}$ dimer system $TlCuCl_3$ [31] and the weakly coupled dimer system $KCuCl_3$ [32] signals are observed at energies corresponding to 2 and 2.6 J, respectively. This result corresponds well to the energy separation between the singlet ground state and the excited triplet. As already noticed in the calculation of the magnetic susceptibility of $S=\frac{3}{2}$ dimers the situation is more complex and excited states exist at 2, 6 and 12 J. For $CoSb_2O_3Br_2$ the mode has an onset at 24 cm^{-1}, a maximum at $E_{max}=37.4\,cm^{-1}$ and a very gradual high energy fade out at 45 cm^{-1}. These energies correspond to the respective multiples of the intra-dimer coupling: 7.7, 12, and 14.4. This surprisingly good agreement should be taken with caution as inter-dimer interaction and the overlap with the phonon at 30.5 cm^{-1} has been neglected. Still the low energy Raman scattering complies with the magnetic energy scales quite well.

The increase of the number of observed modes without coincident frequency shift points to a quite moderate change of the lattice symmetry that modifies the selection rules. The most probable modification is a loss of inversion symmetry lifting the exclusion of Raman- and IR active modes. The number of low-temperature observed modes fully supports this scenario. Following from the temperature dependence of the phonon intensities this moderate structural change happens below approximately 6 K. This temperature scale is between the antiferromagnetic ordering temperature and anomalies at approximately 3 K deduced from specific heat. Therefore, we conclude an additional structural instability in $CoSb_2O_3Br_2$ at lowest temperatures.

4. Conclusions

Single crystals of $CoSb_2O_3Br_2$ have been synthesized via a vapour–solid reaction starting with a mixture of $CoBr_2$ and Sb_2O_3 in stoichiometric molar ratio. The crystal structure contains layers which extend in the *ac*-plane, being separated by non-bonding volumes that are occupied by bromide ions together with unshared electron pairs. These structural features are common in transition metal–lone-pair element–oxo-halide systems. In comparison to similar systems containing Sb^{3+}, a comparatively short Sb–Br bonding distance is found leading to the formation of the uncommon coordination polyhedron $[SbO_3Br]$. The structural peculiarity is the formation of isolated Co–Co dimers made up of two edge sharing distorted $[CoO_4Br_2]$ octahedra. The present compound is to our best knowledge the first described in the Co^{2+}–Sb^{3+}–O–*X* system (*X* = halide anion).

Magnetic susceptibility measurements show that above ~25 K the magnetic susceptibility can be very well described by Curie–Weiss law. Long-range antiferromagnetic ordering observed below T_N~9 K indicates that $CoSb_2O_3Br_2$ contains magnetic dimers, however, with essential inter-dimer coupling within the

layers. To these energy scales the onset of a structural distortion for $T<6$ K in Raman scattering with a concomitant anomaly in the specific heat is added. We attribute the large number of closely distributed critical temperatures to the low symmetry of the system that can be traced back to the topological activity of the lone pair ions.

Supplementary material has been sent to Fachinformationzentrum Karlsruhe, Abt. PROKA, 76344 Eggenstein-Leopoldshafen, Germany (Fax: +49 7247 808 666; E-mail: crysdata@fiz-karlsruhe.de), and can be obtained on quoting the deposit number CSD-418 858.

References

[1] M. Johnsson, K.W. Törnroos, F. Mila, P. Millet, Chem. Mater. 12 (2000) 2853–2857.
[2] M. Johnsson, K.W. Törnroos, P. Lemmens, P. Millet, Chem. Mater. 15 (2003) 68–73.
[3] R. Becker, M. Johnsson, R.K. Kremer, P. Lemmens, J. Solid State Chem. 178 (2005) 2024–2029.
[4] R. Takagi, M. Johnsson, V. Gnezdilov, R.K. Kremer, W. Brenig, P. Lemmens, Phys. Rev. B 74 (2006), 014413/1–014413/8.
[5] R. Takagi, M. Johnsson, R.K. Kremer, P. Lemmens, J. Solid State Chem. 179 (2006) 3763–3767.
[6] R. Becker, M. Johnsson, R.K. Kremer, H.-H. Klauss, P. Lemmens, J. Am. Chem. Soc. 128 (2006) 15469–15475.
[7] D. Zhang, M. Johnsson, Acta Cryst. E64, i26.
[8] J. Zemann, Monatsh. Chem. 102 (1971) 1209–1216.
[9] Z. Mayerová, M. Johnsson, S. Lidin, Angew. Chem. 45 (2006) 5602–5606.
[10] Z. Mayerová, M. Johnsson, S. Lidin, J. Solid State Chem. 178 (2005) 3471–3475.
[11] K. Hanke, V. Kupcik, O. Lindqvist, Acta Cryst. B 29 (1973) 963–970.
[12] J. Deisenhofer, R.M. Eremina, A. Pimenov, T. Gavrilova, H. Berger, M. Johnsson, P. Lemmens, H.-A. Krug von Nidda, A. Loidl, K.-S. Lee, M.-H. Whangbo, Phys. Rev. B 74 (2006), 174421/1–174421/8.
[13] Oxford diffraction, CrysAlis Software (CCD and RED) system, Version 1.171.31.5. Software for the integration of the reflection intensities and absorption correction, 2006.
[14] G.M. Sheldrick, SHELXS-97—Program for the solution of Crystal Structures, Göttingen, 1997.
[15] G.M. Sheldrick, SHELXL-97—Program for the refinement of Crystal Structures, Göttingen, 1997.
[16] K. Brandenburg, DIAMOND, Crystal Impact GbR, Bonn, Germany, 2000, Release 2.1e.
[17] K.E. Johansson, T. Palm, P.E. Werner, J. Phys. E: Sci. Instrum. 13 (1980) 1289–1291.
[18] P.E. Werner, Ark. Kemi 31 (1969) 513–516.
[19] Z. Mayerova, M. Johnsson, S. Lidin, Solid State Sci. 8 (2006) 849–854.
[20] R.J. Gillespie, I. Hargittai, The Vsepr Model of Molecular Geometry, Allyn & Bacon, New York, 1991.
[21] E. Kroumova, M. Aroyo, J.M. Perez-Mato, A. Kirov, C. Capillas, S. Ivantchev, H. Wondratschek, Phase Transitions 76 (1–2) (2003) 155–170 〈http://www.cryst.ehu.es/rep/sam.html〉.
[22] P.W. Selwood, Magnetochemistry, Interscience, New York, 1956.
[23] M.E. Fisher, Philos. Mag. 17 (1962) 1731–1743.
[24] R.L. Carlin, Magnetochemistry, Springer, Berlin, 1986;
H. Lueken, Magnetochemie, TeubnerVerlag, 1999.
[25] H. Lueken, Magnetochemie, TeubnerVerlag, 1999.
[26] I.D. Brown, D. Altermatt, Acta Crystallogr. Sect. B: Struct. Sci. B 41 (1985) 244–247.
[27] I.D. Brown, Bond valence sum parameters 〈http://www.ccp14.ac.uk/ccp/web-mirrors/i_d_brown/bond_valence_param/〉.
[28] C. Hormillosa, S. Healy, Bond valence calculator, Hamilton, Ontario, Canada, 1993 (Version 2.00).
[29] Phonon frequencies fitted at $T=10$ K are: 37.4 (very broad structure), 56.3, 79.9, 90.8, 95.2, 104.8, 111.5, 136, 138.8, 158.8, 185, 199.3, 208.6, 221.2, 228.5, 242.5, 269.4, 281.4, 292, 303.6, 414.1, 536.1, 546.5, 570.2, 602.4, 618.2, 648.7, 688.4.
[30] Additional phonon frequencies fitted at $T=3.1$ K data are: 30.5, 53.5 (split-off from 56.4), 69.4, 76.1, 85.7, 99.2, 107.9, 126.5, 172.4, 192.8, 206.2, 250.3, 309.2 (split-off shoulder), 359.5, 380.4, 461.3.
[31] K.-Y. Choi, G. Güntherodt, A. Oosawa, H. Tanaka, P. Lemmens, Phys. Rev. B 68 (2003), 174412/1–174412/6.
[32] K.-Y. Choi, A. Oosawa, H. Tanaka, P. Lemmens, Phys. Rev. B 72 (2005), 024451/1–024451/5.